RESEARCH ARTICLE

NANO · MICRO small
www.small-journal.com

Construct Stable Charge Carrier Transport Interface for High-Energy-Density Electrodes by Grafting Ion-Conducting Group to Carbon Nanotube Additives

*Nan Meng, Yunfei Du, Bo Pang, and Fang Lian**

Carbon materials are the key additives for electronic conductivity in electrodes, which determine the electrochemical performances and durability of batteries. Herein, a strategy for grafting ion-conducting groups to multi-wall carbon nanotubes (MWCNTs) is proposed via in situ polymerization induced by a Lewis acid agent BF_3, which is generated from the disproportionation of $LiBC_2O_4F_2$ (LiODFB). The as-obtained MWCNTs demonstrate a narrower particle size distribution in the solution due to the reduced surface defects and steric effect between the grafted oxyethylene (EO) segments. Moreover, the MWCNTs with ion-conducting groups (CNT-EO) show not only good electronic/ionic dual conductivity but also high chemical- and electrochemical- stability up to 4.8 V with the $LiNi_{0.8}Co_{0.1}Mn_{0.1}O_2$ (NCM811) electrode. The CNT-EO integrates the cathode into a monolithic structure through an interconnected 3D dual conductive network, which accelerates the construction of a robust LiF-dominated interphase layer on NCM811. Therefore, the Li/NCM811 cells with CNT-EO additive deliver a high discharge capacity of 183.5 mAh g^{-1} at 0.5 C, and a significantly improved cycle life of 400 cycles. The strategy of grafting special functional groups to the CNTs is beneficial to construct a stable charge carrier transport interface for electrodes with high-energy density, long life, and high safety.

1. Introduction

The lithium-ion battery demand is expected to continue to skyrocket for large-scale stationary storage and electric vehicles.[1] In a decade, the technical progress on active materials has contributed greatly to the service performance and cost-effectiveness of lithium-ion batteries.[2,3] But developing the Ni-rich $LiNi_xCo_yMn_zO_2$ (NCM, $x \geq 0.8$, $x+y+z=1$) or Silicon-based electrode with a high loading toward high energy density is quite challenging.[4] For example, during the process of deep delithiation and repeat lithiation in NCM, the mechanical stress caused by the inhomogeneous and anisotropic volume change of primary particles could induce intergranular cracks along the internal grain boundaries and secondary particle fragmentation.[5] The resultant loss in mechanical contact between the active materials in polycrystalline powder, carbon additives and polymer binders blocks the ionic and electronic percolation pathways, causing an impedance increase and performance decay.[6] Therefore, it is noted that the further electrochemical optimization of the batteries depends eventually on the mechanically stable electrode. Strategies for the stable electronic and ionic transfer interface in the electrode have been developed in order to guide the current redistribution, reduce the polarization growth, and enhance the durability of the batteries.[7] Xu et al.[8] built a (Li/Al/Co)(O/F) rock-salt interphase with the cationic/anionic disorder on the surface of $LiCoO_2$ to improve the electron/Li^+ conductivity, which therefore delivered an initial capacity of 154 mAh g^{-1} and 93.0% capacity retention after 1000 cycles at 10 C in 3.0–4.5 V. Fan et al.[9] integrated a robust 3D network using a sodium-superion-conductor-type $Li_{1.4}Y_{0.4}Ti_{1.6}PO_4$ layer on the surface of single-crystal NCM particles, which increased Li^+ and electron conductivity of ≈1.5 and 1.3 times respectively, leading to an improved capacity of 130 mAh g^{-1} after 500 cycles at 5 C in 2.75–4.40 V. Surface modification of active materials not only stabilizes the interface but also facilitates Li^+ and electron conduction in the short-range within the electrodes. Moreover, the homogeneous distribution of conductive additives/binders and their good contact with the active materials powder are vital to achieving high charge transport channels both in the short-range and the long-range for reliable redox reactions of the electrodes,[10–12] which governs the structural integrity of the electrode throughout cycling. Meanwhile, the minimalized content of inert additives contributes to the high active material ratio of the electrodes for the high-energy-density batteries.[13]

Carbon nanotubes (CNTs) demonstrate a lower percolation threshold due to their high aspect ratio.[14] In detail, CNT additives with a smaller amount can ensure electrical contact with

N. Meng
National School of Elite Engineering USTB
University of Science and Technology Beijing
Beijing 100083, China

N. Meng, Y. Du, B. Pang, F. Lian
School of Materials Science and Engineering
University of Science and Technology Beijing
Beijing 100083, China
E-mail: lianfang@mater.ustb.edu.cn

The ORCID identification number(s) for the author(s) of this article can be found under https://doi.org/10.1002/smll.202503375

DOI: 10.1002/smll.202503375

each other either by electron tunneling or direct contact, leading to a sharp rise in the electronic conductivity of the electrode.[15] Moreover, CNTs with robust linear morphology have been proven to achieve better electrode performance compared to carbon black.[16] Among them, single-walled carbon nanotubes (SWCNTs) are shown to be a simple yet effective additive, for example, improving electrical connectivity and increasing capacity retention in the electrodes with high energy density but huge volumetric change.[17] By contrast, multi-walled carbon nanotubes (MWCNTs) are less expensive but are often short with much less adhesion strength. He et al. compared the impact of SWCNTs and MWCNTs with different aspect ratios on the performance of Si-based anodes.[18] The result showed that the long MWCNTs contributed to a better anode performance than the short SWCNTs, owing to the acupuncture effect of the short rigid CNTs on the solid-electrolyte interphase and the carbon layers of the Si-based anodes. The exposed surface of active material accelerates continuous detrimental side reactions with electrolytes, hindering Li^+ diffusion on the interface. Therefore, rather than the number of carbon layers of the CNTs, the improvement of flexibility and distribution of CNTs is much more important as conductive additives, which improve the mechanical stability of the electrodes.

In our work, a novel strategy for ion-conducting oxyethylene (EO) group-grafted to MWCNTs (CNT-EO) was proposed via in situ polymerization. **Scheme** 1a shows the synthesis process of CNT-EO: the trace amounts of Lewis acid BF_3 are generated from the disproportionation of lithium oxalyldifluoroborate (LiODFB) at 60 °C,[19–21] which induces the ring-opening reaction of the epoxy group on ethylene glycol diglycidyl ether (EGDE) by the cationic polymerization. Therefore, ion-conductive EO groups are grafted to carboxylic acid-functionalized MWCNTs in the presence of LiODFB, meanwhile, the EO groups maintain a high dielectric constant and strong Li^+ solvating ability.[22] The as-prepared CNT-EO is dispersed homogeneously and keeps close contact with the active materials during cycling, which integrates the cathode into a monolithic structure. Moreover, a robust LiF-dominated cathode-electrolyte interphase (CEI) layer is induced by CNT-EO, which stabilizes the interface and maintains the structural integrity of the $LiNi_{0.8}Co_{0.1}Mn_{0.1}O_2$ (NCM811) electrode. The CNT-EO addition can ensure a continuous charge transfer pathway for NCM811 cathode during cycling. Therefore, the Li/NCM811 batteries with CNT-EO display a stable cycle performance for more than 400 cycles with a high-capacity retention of 70.08%, as well as a good rate capacity of 141.77 mAh g^{-1} at 3.0 C.

2. Results and discussion

The weight ratio of EGDE grafted to MWCNTs is measured by Thermogravimetric analyzer (TGA) in **Figure** 1a. EGDE exhibits a sharp weight loss starting at 131.51 °C, while MWCNTs show thermal stability up to 600 °C. The weight ratio of MWCNTs: EGDE is determined to be 4:1 and 1:1, therefore the samples are named as CNT-EO-41 and CNT-EO-11, respectively (Table S1, Supporting Information). The decomposition temperature gradually decreases with an increase in ion-conducting EO content. The CNT-EO-11 samples demonstrate thermal stability below 186.56 °C and CNT-EO-41 with an appropriate amount of ion conductive segments demonstrates a higher decomposition temperature at 239.37 °C.

The morphologies of CNTs before and after grafting are shown in Figure 1b–d and S1 (Supporting Information). In the scanning electron microscopy (SEM) image, CNT-EO-41 still keeps the morphology of CNTs, while CNT-EO-11 is fully covered by amorphous polymer. The transmission electron microscope (TEM) image of CNT-EO-41 in Figure 1d shows a small amount of amorphous polymer coated on the part of the CNTs.

Fourier transform infrared spectroscopy (FTIR) was conducted to analyze the surface chemical structure of the carbon materials. Figure 1e shows the FTIR spectra of MWCNTs and CNT-EO-41. The peaks at 1631, 1543, and 1164 cm^{-1} correspond to C═O, C═C, and C—C stretching vibrations of the carbon backbone, respectively. In the CNT-EO-41 spectra, the vibration peak belonging to the hydroxyl group at 3447 cm^{-1} appears, and simultaneously the absorption peak at 911 cm^{-1} of the epoxy groups disappears as in Figure S2 (Supporting Information), which indicates that the epoxy group in EGDE is attached to the carboxyl group on CNT through ring opening reaction.[23] The increased intensity of the C—H vibrational peak at 2920 cm^{-1} is attributed to the C—H stretching in -CH_2 for the CNT-EO-41 carbon materials, while the vibrational peak ≈1100 cm^{-1} corresponds to the C—O—C group (Figure S3, Supporting Information),[2,24] which implies that the chain segments graft to MWCNTs by in situ polymerization after ring-opening reaction of EGDE.

The Raman spectra in Figure 1f demonstrate the high-intensity ratio of 1.28 between the D band (1384 cm^{-1}) and G band (1595 cm^{-1}) (ID/IG) of MWCNTs with defects, which could be used for functional modification. The ID/IG values of MWCNTs and CNT-EO-41 are 1.28 and 1.17, respectively, indicating that the EO-grafting decreases the surface defects of MWCNTs. High-resolution X-ray photoelectron spectroscopy (XPS) was further used to investigate the surface chemical state. The deconvolution of C 1s spectra in Figure 1g,h and Figure S4 (Supporting Information) reveals four peaks, corresponding to graphitized carbons (284.8 eV), C═C (285.2 eV), C—O (285.9 eV), and C═O (289.1 eV).[25] The peak intensities of C—O in CNT-EO-41 and MWCNT-EO-11 are significantly higher than that of the CNT sample, corroborating that ion conductive EO segments graft onto the surface of carbon materials.

Dynamic light scattering (DLS) analysis in Figure 1i shows that MWCNTs have an average hydrodynamic particle diameter of 14.2 μm, which is smaller than the average length of MWCNTs due to the convolution of the long tubes. In comparison, the CNT-EO-41 sample exhibits a remarkably reduced particle diameter of 11.8 μm, indicating a better dispersion state than MWCNTs as shown in Scheme 1, which is attributed to the reduced defects of MWCNTs and steric hindrance effect between the organic segments on the surface.[26] However, excessive EO segment on the surface of CNT-EO-11 (Figure S5, Supporting Information) might cause the crosslinking mutually, leading to an increase in the average particle size of CNTs.

The electrostatic potential calculation demonstrates an increase in the density of the electron cloud around the epoxy group of EGDE, which corroborates the epoxy group of EGDE with much stronger electronegativity than the carboxylic acid functional groups on CNT (Figure S6, Supporting Information).[27]

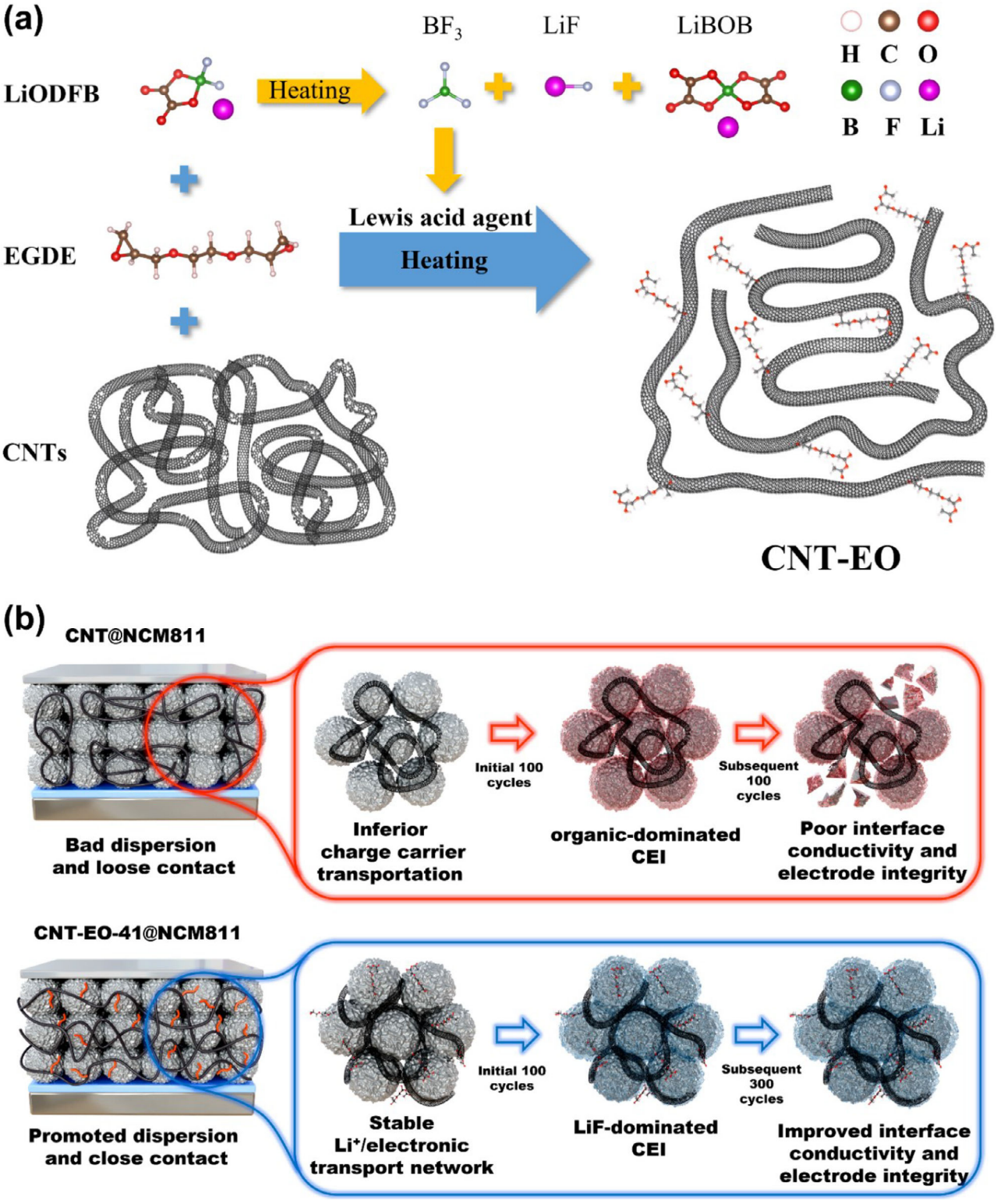

Scheme 1. a) Schematic illustration of the cationic polymerization mechanism of CNT-EO. b) Schematic illustration of the cathode evolution in CNT@NCM811 and CNT-EO-41@NCM811 batteries.

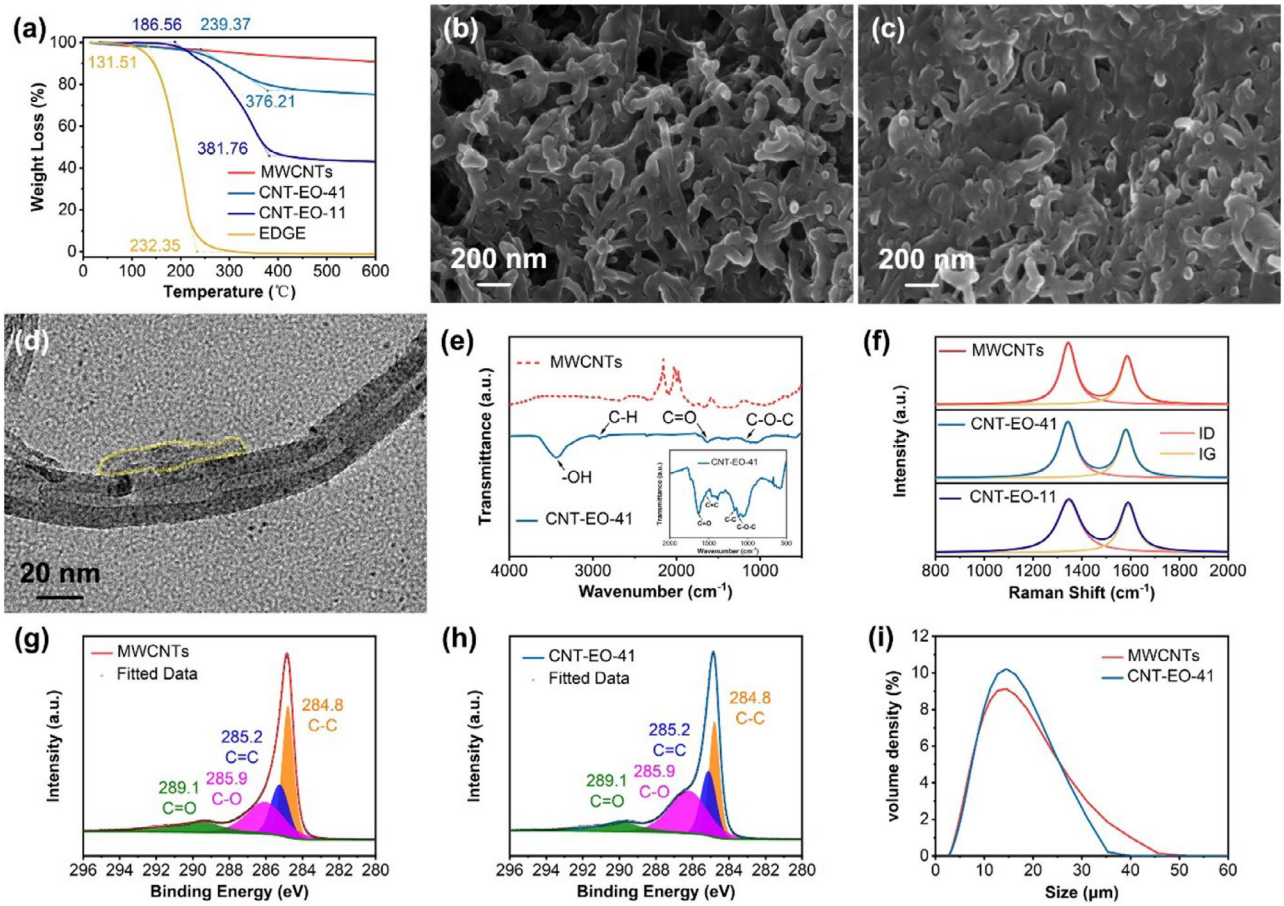

Figure 1. a) TGA results of the EGDE and CNTs. Morphologies of CNTs: SEM image of b) MWCNTs and c) CNT-EO-41, d) TEM image of CNT-EO-41. e) FTIR of MWCNTs and CNT-EO-41. f) Raman spectra of MWCNTs, CNT-EO-41 and CNT-EO-11, C 1s XPS spectra of g) CNTs and h) CNT-EO-41. i) Particle size distribution of CNTs and CNT-EO-41.

The trace amounts of Lewis acid BF_3 generated from the disproportionation of LiODFB at 60 °C initiate the ring-opening reaction of the electronegative epoxy group in EGDE, ending up with the grafting of the EO segments on the carboxylic acid functional groups of MWCNTs.[19–21] Together with FTIR, TGA, Raman, and XPS analysis, the calculation and experiment results corroborate that the EO segment of EGDE grafting to MWCNTs is realized in the presence of LiODFB.

In addition, in solid polymer electrolytes, EO chains are recognized as efficient Li^+ conductors due to their strong polarity, excellent flexibility, and facile chemical modifiability.[28] These inherent advantages motivated the strategic selection of EO segments for grafting to MWCNTs, thereby achieving enhanced electronic/ionic dual conductivity of the carbon-based material. As shown in Figure S6 (Supporting Information), strong negative electrostatic potential in EO chains implies that the oxygen atom induces the interaction with Li^+, which could accelerate Li^+ transport kinetics.

The electronic conductivity of the solid cathode pellets containing CNT-EO-41 is determined to be 7.94×10^{-3} S cm^{-1}, which is much higher than that of the cathode pellets with MWCNTs (4.22×10^{-3} S cm^{-1}) (**Figure 2a**). Moreover, the ionic conductivity of the CNT-EO-41@$LiFePO_4$ (LFP) cathode pellets reaches 2.83×10^{-4} S cm^{-1} (Figure 2b), which is much higher than that (8.29×10^{-5} S cm^{-1}) of CNT@LFP cathode pellet (the detail impedance spectra are given in Figure S7 and S8 (Supporting Information). The π-electron localized orbital locator (LOL-π) was performed to evaluate the influence of the ion conductive segments on CNTs. In Figure 2c,d, CNTs demonstrate a higher density of π electrons of the interior than the exterior, in which the isosurface over each carbon atom on the outer layer is fully isolated, while some neighboring carbon atoms in the inner layer show a merged isosurface.[29] Moreover, the high delocalization LOL-π regions in the CNT-EO samples (red color regions) reveal the favorable delocalization path in the LOL-π color-filled map (Figure 2e; Figure S9, Supporting Information).[30] The above calculation corroborates that grafting ion conductive EO segments on the surface of MWCNT improves its electron delocalization path and the overall conjugation effect of CNT-EO-41.

The linear sweep voltammetry (LSV) test was performed to investigate the electrochemical window of CNT-EO-41 in Figure 2f. CNT-EO-41 is stable up to 6.0 V without any current fluctuation. Furthermore, as shown in Figure 2g and Figure S10 (Supporting Information), the oxidation stability of the electrodes with CNT-EO-41 is evaluated by an electrochemical floating experiment. The LFP, $LiCoO_2$ (LCO), and NCM811 batteries with

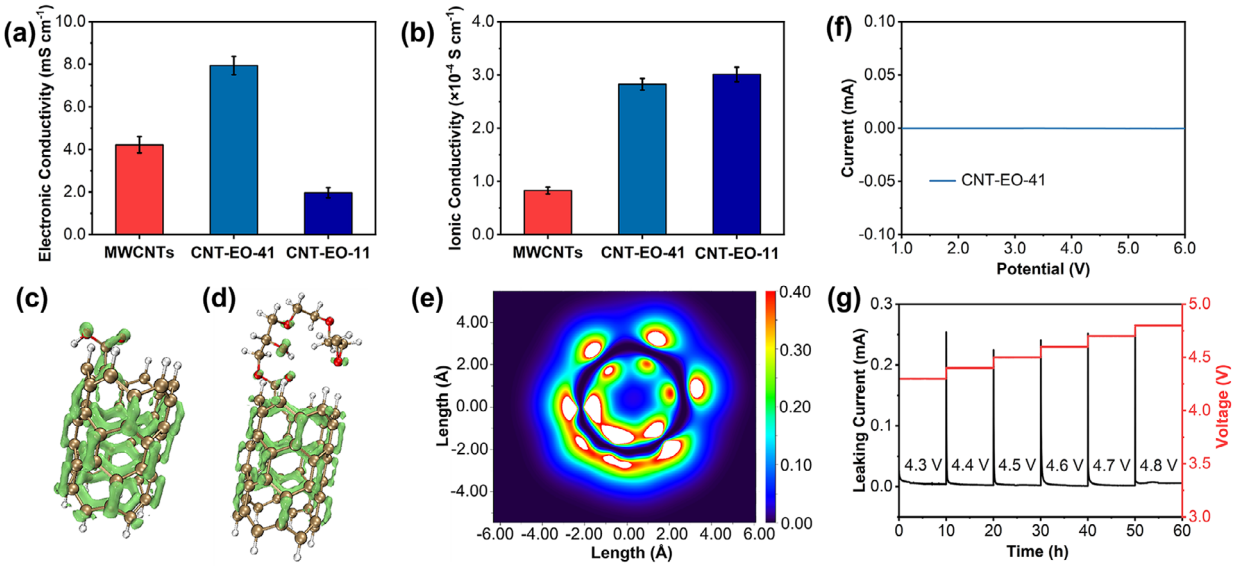

Figure 2. The electronic a) and ionic b) conductivities of CNT@LFP, CNT-EO-41@LFP, and CNT-EO-11@LFP cathodes. The LOL-π isosurface map of c) CNT and (d) CNT-EO. e) The LOL-π color-filled map of CNT-EO. f) LSV plots of CNT-EO-41. g) Electrochemical floating analysis of the NCM811 cells assembled with CNT-EO-41.

CNT-EO-41 display limited leakage current and remain stable at 4.8 V, which demonstrates excellent electrochemical stability of CNT-EO-41 and its compatibility with the LFP, LCO, and NCM811 active materials.

In general, an appropriate amount of ionic conductive chain segments produces a steric hindrance effect, promoting the dispersion and also delocalizing π electrons of MWCNTs, which ends up with an enhanced electronic and ionic conductivity of the electrode. Accordingly, the CNT-EO-41 with MWCNTs: EGDE ratio of 4:1 delivers high electronic and ionic conductivity simultaneously, and superior electrochemical stability even with NCM811, which is chosen as the optimal additive for NCM811 electrode evaluations in lithium-ion batteries for its high energy density.

The NCM811 cathode with active material weight ratio increased to 90% was evaluated in **Figure** 3a,b. The NCM811 cathodes with CNT-EO-41 and MWCNTs as conductive agents were labeled as CNT-EO-41@NCM811 and CNT@NCM811. CNT@NCM811 and CNT-EO-41@NCM811 cells deliver an initial discharge capacity of 185.3 and 183.5 mAh g^{-1} at 0.5 C, respectively. After 240 cycles, the CNT@NCM811 electrodes deliver a specific discharge capacity of 137.6 mAh g^{-1} with a capacity retention of 74.28%, while the CNT-EO-41@NCM811 electrode exhibits a specific discharge capacity of 146.9 mAh g^{-1} with a capacity retention of 80.05%. After the 400th cycle, CNT@NCM811 only shows a capacity retention of 51.38%, while CNT-EO-41@NCM811 shows a capacity retention of 70.08%. Moreover, the rate performance of CNT-EO-41@NCM811 has been shown in Figure 3b, which exhibits discharge capacity of 175.91 mAh g^{-1}, 161.76 mAh g^{-1}, 141.77 mAh g^{-1}, 111.07 mAh g^{-1} and 75.06 mAh g^{-1} at the rate of 1.0 C, 2.0 C, 3.0 C, 4.0 C and 5.0 C, respectively. The discharge capacity was restored to 200.47 mAh g^{-1} when the current density decreased from 5.0 C to 0.1 C, showing an excellent rate performance of CNT-EO-41@NCM811. While, as in Figure S11 (Supporting Information), the discharge capacity of CNT@NCM811 at 1.0, 2.0, 3.0 and 4.0 C are 170.27 mAh g^{-1}, 124.32 mAh g^{-1}, 73.51 mAh g^{-1} and 1.98 mAh g^{-1}, which is inferior to CNT-EO-41@NCM811 owing to the worse electronic and ionic conductivity of the cathode.

To investigate the effect of conductive additives on the cathode, the electrochemical impedance spectroscopy characterization of the Li/NCM811 cells after activation and 100 cycles was performed in Figure 3c and Figure S12 (Supporting Information). With the higher electronic and ionic conductivity, CNT-EO-41@NCM811 shows a smaller bulk resistance of 4.4 Ω versus 7.7 Ω of CNT@NCM811. Moreover, compared with CNT@NCM811 (742.9 Ω), CNT-EO-41@NCM811 after 100 cycles demonstrates a smaller semicircle at the mid-frequency region in the Nyquist plot, corresponding to a lower impedance of 412.1 Ω. The Li^+ diffusion coefficient of the CNT-EO-41@NCM811 batteries from the galvanostatic intermittent titration technique (GITT) is higher than that of CNT@NCM811 as shown in Figure 3d,e and S13 (Supporting Information). The morphology of NCM811 cathodes before and after 200 cycles was characterized by SEM in Figure 3f–k and S14 (Supporting Information). The disassembled CNT-EO-41@NCM811 electrodes still maintain the original morphology, and the secondary particles exhibit a uniform and compact interface without any significant cracks or exposures after cycles. In contrast, several cracks and breaks are detectable on the surface of the secondary particles in the CNT@NCM811 electrode, which attributes to a significant capacity loss in the long-term cycles. Due to the improved interface conductivity and electrode integrity, the NCM811 cathode with CNT-EO-41 exhibits better electrochemical performance in comparison with the recent reports as shown in Table S2 (Supporting Information).

During the cycling of the batteries, CEI will be generated on the interface between the cathode material and electrolyte, which is investigated herein using XPS and Time-of-flight secondary ion mass spectrometry (TOF-SIMS) after 100 cycles at 0.5 C of the CNT@NCM811 and CNT-EO-41@NCM811

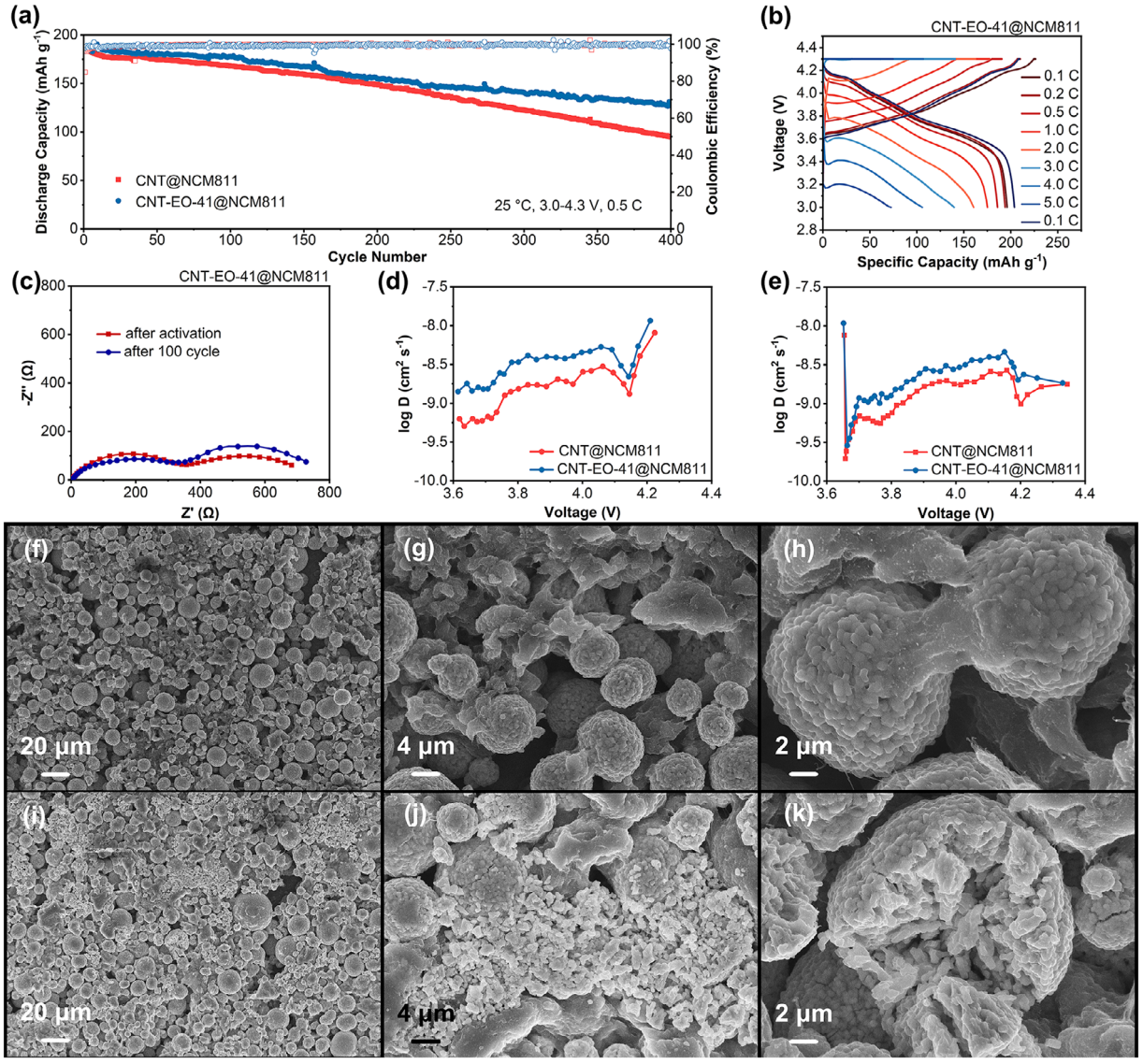

Figure 3. a) The cycling performance of CNT@NCM811 and CNT-EO-41@NCM811 at room temperature at 0.5 C between 3.0–4.3 V (vs Li/Li^+). b) The charge–discharge voltage profiles of CNT-EO-41@NCM811 at different rates from 0.1 C to 5.0 C between 3.0–4.3 V (vs Li/Li^+). c) Impedance spectra of CNT-EO-41@NCM811 after activation and after the 100th cycle. Diffusion coefficients from the GITT potential profiles for CNT@NCM811 and CNT-EO-41@NCM811 as a function of the state of d) charge and e) discharge. SEM images at different magnifications of f–h) CNT-EO-41@NCM811, and i–k) CNT@NCM811 after 200 cycles at 0.5 C between 3.0–4.3 V (vs Li/Li^+).

cathodes. The F 1s spectra of the cathodes after cycling are shown in **Figure** 4a,b. The CNT-EO-41@NCM811 cathode shows a significantly improved ratio of Li-F peak at 685.4 eV versus C-F peak (corresponding to the PVDF binder) at 687.6 eV,[31] which demonstrates a Li-F dominated CEI on the CNT-EO-41@NCM811 compared with CNT@NCM811. Furthermore, a thorough analysis of the CEI layer was conducted by TOF-SIMS. In the TOF-SIMS depth profiles, NiO^- fragment represents NCM811 bulk, LiF_2^- and C_2HO^-/CH_2O^- fragments are in association with the inorganic species and organic species from the decomposition of the electrolyte respectively, while NiF_3^- fragment stands for the dissolved active materials. Both CNT@NCM811 and CNT-EO-41@NCM811 in Figure 4c,d demonstrate similar intensity increments of the NiO^- fragment, indicating a comparable CEI thickness on both cathodes (assuming that the edge of the CEI layer corresponds to an increase in normalized intensity of NiO^- to 80%).[32] Moreover, as shown in Figure 4c,d, the much more LiF-intensive CEI layers are formed on the CNT-EO-41@NCM811 cathode in comparison with CNT@NCM811, which is also indicated by the LiF_2^- 3D distributions in Figure 4g. Conversely, the C_2HO^-/CH_2O^- fragments in CNT@NCM811 are more dominant than CNT-EO-41@NCM811, as observed from Figure 4e and h, showing an organic-specie dominated CEI on CNT@NCM811. Moreover, CNT@NCM811 exhibits signs of transition metal dissolution after 100 cycles in Figure 4f. Therefore, the CNT-EO-41-induced robust CEI prevents the cathode materials from collapsing, improving the durability of the high-energy-density batteries.[33]

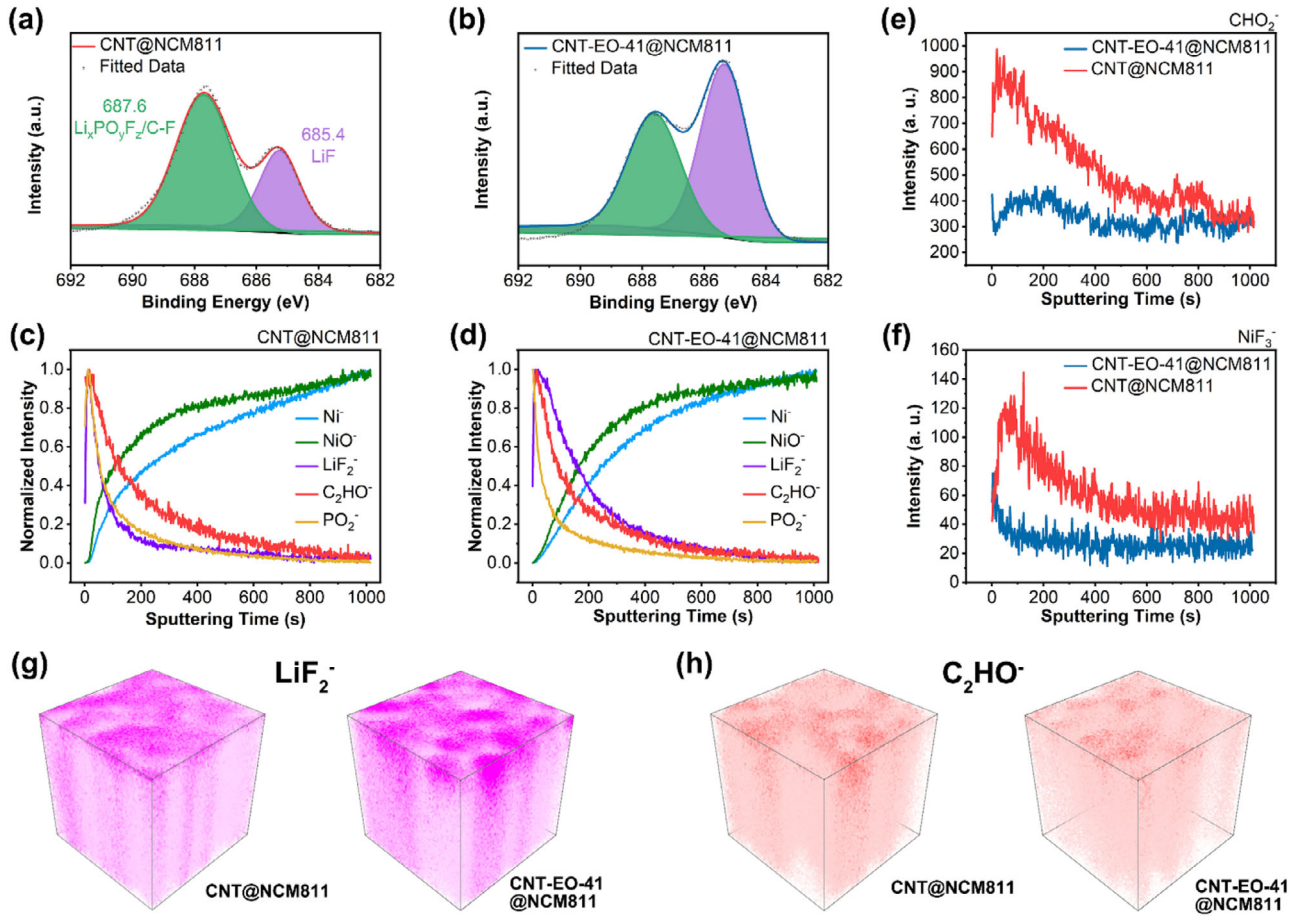

Figure 4. F 1s XPS spectra of a) CNT@NCM811 and b) CNT-EO-41@NCM811 after 100 cycles at 0.5 C between 3.0–4.3 V (vs Li/Li^+). Normalized TOF-SIMS depth profiles of the CEI layers on c) CNT@NCM811 and d) CNT-EO-41@NCM811 after 100 cycles at 0.5 C between 3.0–4.3 V (vs Li/Li^+). TOF-SIMS depth profiles of different fragments on CNT@NCM811 and CNT-EO-41@NCM811 after 100 cycles: e) CHO_2^- and f) NiF_3^-. 3D distributions of different fragments on CNT@NCM811 and CNT-EO-41@NCM811 after 100 cycles: g) LiF_2^- and (h) C_2HO^-.

The interaction between the electrolyte and CNT-EO was studied using the classic molecular dynamic simulations as in Figure S15 (Supporting Information). The grafted EO groups are directly solvate with Li^+, pulling the Li^+ with PF_6^- in its solvation structure to the vicinity of the CNT-EO, which not only accelerates Li^+ conduction on the electrolyte/electrode interface but also facilitates to the formation of a LiF-dominant CEI layer.

In conclusion, the CNT-EO with ion-conducting segment grafting to the surface demonstrates the promoted dispersion and close contact with Ni-rich layered material as depicted in Scheme 1b integrating the cathode into a monolithic structure, which increases particle interconnectivity due to the high tensile strength carbon nanotubes. Moreover, CNT-EO-41@NCM811 exhibits a robust and more conductive LiF-dominant CEI layer.[34] In contrast, the CEI layer on CNT@NCM811 is primarily composed of organic species derived from the decomposition of carbonate solvents, which exhibits lower conductivity.[35] Therefore, CNT-EO additive constructs a stable Li^+/electronic transport network within the cathode and ensures continuous charge transfer pathways for the electrochemical reaction, which contributes to the improved cycling stability of the NCM811 batteries.

3. Conclusion

A novel strategy of ion-conducting EO group grafted to CNT (CNT-EO) is developed with the aim of a carbon-based electronic and ionic dual conducting additive. The solid-state cathode pellets with CNT-EO-41 exhibit high electronic conductivity (7.94×10^{-3} S cm^{-1}) and ionic conductivity (2.83×10^{-4} S cm^{-1}), as well as remarkable chemical and electrochemical stability up to 4.8 V (vs Li/Li^+). More importantly, the improved dispersion of CNTs, good contact with active materials, and the robust LiF-dominant CEI layer induced on the cathode contribute to constructing a stable and rapid charge carrier transport channel in the cathode, enhancing effectively the ion/electron transport at the cathode/electrolyte interface, ensuring a continuous charge transfer pathway for normal cathodic electrochemical reaction, and suppressing the polarization induced by the ion/electron concentration gradient in the electrodes. The high active loading Li/NCM811 batteries using CNT-EO present much better cycling performance for more than 400 cycles and higher capacity retention of 70.08% at room temperature. This work creates great potential for the economic practical application of MWCNTs additives for high energy density and long lifespan batteries.

4. Experimental Section

Synthesis of CNT-EO Materials: MWCNTs with 3.86% carboxylic acid functional groups (J & K Scientific) were dispersed in methyl pyrrolidone (NMP, Sinopharm) with a weight ratio of 5 wt.% via ultrasound and magnetic stirring. Then, LiODFB (Macklin) and EGDE (Macklin) were added with the LiODFB: EGDE mass ratio of 1:10 to obtain CNTs with the ion conductive segments. The samples named as CNT-EO-41 and CNT-EO-11 were prepared, in which the mass ratio of MWCNTs and EGDE is determined to be 2:1 and 1:4 respectively. The mixture was kept stirring for 12 h in an argon-filled glove box ($H_2O < 0.1$ ppm, $O_2 < 0.1$ ppm) at 60 °C and used directly in the cathode preparation or vacuum-dried at 80 °C for 12 h for material characterization.

Materials Characterization: FTIR measurement was carried out on a Bruker Vector 22 infrared spectrophotometer from KBr pellets between 500 and 4000 cm^{-1}. TGA (Discovery, Waters) was conducted in nitrogen from 50 to 600 °C at a heating rate of 10 °C min^{-1}. Raman measurement was performed with a Raman JY HR800 spectrometer. XPS spectrum was tested on a Phoibos X-ray photoelectron spectrometer (100 Analyzer, SPECS, Germany, Al Kα X-rays). Scanning electron microscopy (SEM) was carried out on a ZEISS SUPRA55, and TEM was performed on a JEOL JEM-2010 microscope. TOF-SIMS was conducted using a TOF.SIMS 5–100 spectrometer (ION-TOF GmbH, Germany) with a primary ion beam of 30 keV Bi_3^+, covering a scan area of 100 × 100 μm^2.

Measurements on the Ionic and Electronic Conductivity of Solid Cathode Pellet: To reveal the contribution of CNT-EO to the electrode, $LiFePO_4$ (LFP) solid cathode pellets with CNT-EO were designed and characterized for the ionic and electronic conductivity via potentiostatic and electrochemical impedance spectroscopy measurements using an electrochemical workstation (VersaSTAT3).[36] In detail, the cathode composite powder with the proportion of LFP:CNT-EO: PVDF = 80:15:5 was uniformly mixed into the NMP solvent to promote the dissociation of Li salt and the coordination of Li^+ with ionic conductive polymer. Then the mixture was vacuum dried at 80 °C for 12 h and subsequently compressed into 10 mm diameter pellets with a thickness of ≈300 µm at ≈4.0 MPa using an isostatic pressing machine and pellet moulds (Xinnuo Instrument). The SS| solid cathode pellet |SS cell was assembled to perform the potentiostatic test with an applied voltage of 50 mV, the steady-state current was recorded. The electronic conductivity was calculated by using the following Equation (1):

$$\sigma_{electron} = \frac{1}{\rho} = \frac{l*I}{s*V} \quad (1)$$

where V is the applied voltage, I is the steady-state current, l is the thickness of the cathode pellet, s represents the contact area between the cathode composite pellet and SS, and ρ is the electrical resistivity of the cathode pellet.

For the ionic conductivity measurement, the solid cathode pellet was sandwiched between two Dual-Li SPE[37] with a thickness of ~30 µm to block the electron transportation to assemble the SS|SPE| cathode pellet |SPE|SS cell as well as SS|SPE|SPE|SS cell, then the impedance measurements were carried out at 30 °C. The ionic conductivity was calculated according to the Equation (2):

$$\sigma = \frac{L}{SR} \quad (2)$$

where L is the thickness of the cathode pellets, S represents the surface area of the stainless steel, and R is the measured resistance.

Electrochemical Measurements: The electrochemical stability window of CNT-EO without cathode material was measured using a LSV experiment performed on a working electrode with lithium anode as a counter and reference electrode at a sweep rate of 1 mV s^{-1} between 0 and 6.0 V with an electrochemical workstation (VersaSTAT3).

The cathode slurry was prepared by mixing active material NCM811, CNT-EO-41, and PVDF in NMP with the mass ratio of 90:5:5 at 60 °C for 6 h. The mixed slurry was cast onto aluminum foil and dried in a vacuum at 80 °C for 12 h. The cathode with active material loading ≈3 mg cm^{-2} was cut into discs with a diameter of 12 mm for cell assembly. The coin cells were assembled in an Ar-filled glovebox with $LiPF_6$ (1 mol L^{-1}) dissolved in a mixed solution of ethylene carbonate (EC), dimethyl carbonate (DMC), and diethyl carbonate (DEC) (EC:DMC: DEC = 1:1:1 in volumetric ratio) as electrolyte and lithium metal as anodes. Electrochemical floating test was proceeded by charging the Li/LFP, Li/LCO, and Li/NCM811 cell to 4.25 V (Li/LFP), 4.4 V (Li/LCO) and 4.3 V (Li/NCM811) at a constant current of 0.05 C and subsequently charging at constant voltage for 10 h between 4.3–4.8 V (Li/LFP), 4.4–4.8 V (Li/LCO) and 4.3–4.8 V (Li/NCM811) with a battery test system (CT-3008-164, NEWARE). Galvanostatic charge-discharge tests of Li/NCM811 batteries were performed between 3.0 and 4.3 V on a Land CT2001A automatic battery test system at different current rates at 30 °C. Li/NCM811 cells were cycled at 0.5 C followed by activation at 0.1 C in the initial three cycles (1.0 C = 180 mA g^{-1}).

Calculation Methods: All quantum chemical calculations in this work were performed with the B3LYP level using the framework of the ORCA 4.0 program.[38] The density functional B3LYP combined with the D3 dispersion correction was employed, and the 6–311G+(d,p) basis set was used for all atoms. Both structural optimization and frequency analysis were performed at the same level of theory. All optimized structures have satisfied the default convergence criteria and exhibit no imaginary frequencies. The point charges on each atom were obtained by fitting the electrostatic potential surface with the RESP (Restrained Electro Static Potential) method using Multiwfn, and the local electronic function graph could be calculated.[39–41] LOL-π were calculated by Multiwfn 3.8 programs,[42] and the isovalue of 0.55 was adapted to distinguish the delocalization extent of the π electrons on different rings.

Supporting Information

Supporting Information is available from the Wiley Online Library or from the author.

Acknowledgements

This work was financially supported by the National Natural Science Foundation of China (No. 52172180), and the China Postdoctoral Science Foundation (No. 2023M730210).

Conflict of Interest

The authors declare no conflict of interest.

Data Availability Statement

The data that support the findings of this study are available from the corresponding author upon reasonable request.

Keywords

additives, carbon nanotubes, energy density, grafting, interphase, lithium-ion batteries

Received: March 15, 2025
Revised: April 18, 2025
Published online: May 8, 2025

[1] H. Z. Niu, N. Zhang, Y. Lu, Z. Zhang, M. N. Li, J. X. Liu, N. Zhang, W. Q. Song, Y. Z. Zhao, Z. C. Miao, *J. Energy Storage* **2024**, *88*, 111666.
[2] H. Li, F. Lian, N. Meng, C. Xiong, N. Wu, B. Xu, Y. Li, *Adv. Funct. Mater.* **2020**, *31*, 2008487.
[3] Y. Du, L. Zhao, C. Xiong, Z. Sun, S. Liu, C. Li, S. Hao, W. Zhou, H. Li, *Energy Storage Mater.* **2023**, *56*, 310.
[4] R. Ruess, S. Schweidler, H. Hemmelmann, G. Conforto, A. Bielefeld, D. A. Weber, J. Sann, M. T. Elm, J. Janek, *J. Electrochem. Soc.* **2020**, *167*, 100532.
[5] P. Minnmann, F. Strauss, A. Bielefeld, R. Ruess, P. Adelhelm, S. Burkhardt, S. L. Dreyer, E. Trevisanello, H. Ehrenberg, T. Brezesinski, F. H. Richter, J. Janek, *Adv. Energy Mater.* **2022**, *12*, 182201425.
[6] R. Koerver, W. Zhang, L. de Biasi, S. Schweidler, A. O. Kondrakov, S. Kolling, T. Brezesinski, P. Hartmann, W. G. Zeier, J. Janek, *Energy Environ. Sci.* **2018**, *11*, 2142.
[7] Y. Zou, Z. Cao, J. Zhang, W. Wahyudi, Y. Wu, G. Liu, Q. Li, H. Cheng, D. Zhang, G. T. Park, L. Cavallo, T. D. Anthopoulos, L. Wang, Y. K. Sun, J. Ming, *Adv. Mater.* **2021**, *33*, 2102964.
[8] S. Xu, X. Tan, W. Ding, W. Ren, Q. Zhao, W. Huang, J. Liu, R. Qi, Y. Zhang, J. Yang, C. Zuo, H. Ji, H. Ren, B. Cao, H. Xue, Z. Gao, H. Yi, W. Zhao, Y. Xiao, Q. Zhao, M. Zhang, F. Pan, *Angew. Chem., Int. Ed.* **2023**, *62*, 202218595.
[9] X. Fan, X. Ou, W. Zhao, Y. Liu, B. Zhang, J. Zhang, L. Zou, L. Seidl, Y. Li, G. Hu, C. Battaglia, Y. Yang, *Nat. Commun.* **2021**, *12*, 5320.
[10] T. DuBeshter, P. K. Sinha, A. Sakars, G. W. Fly, J. Jorne, *J. Electrochem. Soc.* **2014**, *161*, A599.
[11] Z. Ju, X. Xu, X. Zhang, K. U. Raigama, G. Yu, *Chem. Eng. J.* **2023**, *454*, 140003.
[12] M. Ebner, D. W. Chung, R. E. García, V. Wood, *Adv. Energy Mater.* **2014**, *4*, 1301278.
[13] C. D. Quilty, D. Wu, W. Li, D. C. Bock, L. Wang, L. M. Housel, A. Abraham, K. J. Takeuchi, A. C. Marschilok, E. S. Takeuchi, *Chem. Rev.* **2023**, *123*, 1327.
[14] T. Najuch, C. Bierwisch, T. Yamauchi, *Mater. Des.* **2023**, *232*, 112090.
[15] M. Yoshio, R. J. Brodd, A. Kozawa, *Lithium-Ion Batteries: Science and Technologies*, Springer, New York **2009**, 117.
[16] S. H. Tsai, Y. L. Tsou, C. W. Yang, T. Y. Chen, C. Y. Lee, *Electrochim. Acta* **2020**, *362*, 137166.
[17] Z. Y. He, Z. X. Xiao, H. J. Yue, Y. X. Jiang, M. Y. Zhao, Y. K. Zhu, C. H. Yu, Z. X. Zhu, F. Lu, H. R. Jiang, C. X. Zhang, F. Wei, *Adv. Funct. Mater.* **2023**, *33*, 2300094.
[18] Z. Y. He, C. X. Zhang, Y. K. Zhu, F. Wei, *Energy Environ. Sci.* **2024**, *17*, 3358.
[19] Y. Kang, W. Lee, D. Hack Suh, C. Lee, *J. Power Sources* **2003**, *119*, 448.
[20] V. Aravindan, P. Vickraman, K. Krishnaraj, *Polym. Int.* **2008**, *57*, 932.
[21] C. Ma, J. Zhang, M. Xu, Q. Xia, J. Liu, S. Zhao, L. Chen, A. Pan, D. G. Ivey, W. Wei, *J. Power Sources* **2016**, *317*, 103.
[22] H. Wu, B. Tang, X. Du, J. Zhang, X. Yu, Y. Wang, J. Ma, Q. Zhou, J. Zhao, S. Dong, G. Xu, J. Zhang, H. Xu, G. Cui, L. Chen, *Adv. Sci.* **2020**, *7*, 2003370.
[23] Y. Cui, X. Liang, J. Chai, Z. Cui, Q. Wang, W. He, X. Liu, Z. Liu, G. Cui, J. Feng, *Adv. Sci.* **2017**, *4*, 1700174.
[24] H. Li, Y. Du, X. Wu, J. Xie, F. Lian, *Adv. Funct. Mater.* **2021**, *31*, 2103049.
[25] S. Xue, S. Zhao, J. Lu, L. Wu, F. Lian, *ACS Nano* **2022**, *16*, 2651.
[26] J. Ahn, B. Park, J. Kim, M. K. Um, J. W. Yi, J. K. Yoo, *ACS Appl. Mater. Interfaces* **2021**, *13*, 19970.
[27] Y. Wu, Q. Hu, H. Liang, A. Wang, H. Xu, L. Wang, X. He, *Adv. Energy Mater.* **2023**, *13*, 2300259.
[28] N. Meng, F. Lian, G. L. Cui, *Small* **2021**, *17*, 2005762.
[29] T. Lu, Q. Chen, *Theor. Chem. Acc.* **2020**, *139*, 25.
[30] T. Sun, Z. Yi, W. Zhang, Q. Nian, H. J. Fan, Z. Tao, *Adv. Funct. Mater.* **2023**, *33*, 2306675.
[31] Y. J. Cao, N. Li, N. Li, W. J. Zhang, S. Y. Liang, Z. D. Hou, D. Lei, T. Jin, J. G. Wang, K. Y. Xie, C. Shen, *Energy Storage Mater.* **2023**, *60*, 10102851.
[32] H. H. Ryu, H. W. Lim, G. C. Kang, N. Y. Park, Y. K. Sun, *ACS Energy Lett.* **2023**, *8*, 1354.
[33] W. X. Li, Z. X. He, Y. L. Jie, F. Y. Huang, Y. W. Chen, Y. Wang, W. Q. Zhang, X. B. Zhu, R. G. Cao, S. H. Jiao, *Adv. Funct. Mater.* **2024**, *34*, 2406770.
[34] P. X. Bai, X. Ji, J. X. Zhang, W. R. Zhang, S. Hou, H. Su, M. J. Li, T. Deng, L. S. Cao, S. F. Liu, X. Z. He, Y. H. Xu, C. S. Wang, *Angew. Chem.-Int. Edit.* **2022**, *61*, 202202731.
[35] C. Yan, R. Xu, Y. Xiao, J. F. Ding, L. Xu, B. Q. Li, J. Q. Huang, *Adv. Funct. Mater.* **2020**, *30*, 211909887.
[36] M. Zhang, K. F. Zhou, D. H. Ma, H. L. Wang, X. Y. Tang, M. Bai, F. Liu, Z. Q. Wang, Y. Ma, *Mater. Today* **2022**, *56*, 53.
[37] N. Meng, H. Zhang, S. Lianli, F. Lian, *J. Membr. Sci.* **2020**, *597*, 117768.
[38] F. Neese, *Rev.-Comput. Mol. Sci.* **2018**, *8*, 6e1327.
[39] T. Lu, F. Chen, *J. Comput. Chem.* **2012**, *33*, 580.
[40] P. C. Christopher, I. Bayly, W. Cornell, P. A. Kollman, *J. Phys. Chem.* **1993**, *97*, 10269.
[41] J. Zhang, T. Lu, *Phys. Chem. Chem. Phys.* **2021**, *23*, 20323.
[42] T. Lu, F. W. Chen, *J. Comput. Chem.* **2012**, *33*, 580.